Chapter 4

Spectroscopic results

4.1 Valence states of ClF

The valence states are accessed by single photon excitation either with an excimer laser (308 nm), with the second harmonic of the Ti:Sa (387 nm) or the tunable NOPA (330 - 250 nm).

4.1.1 Absorption

Absorption spectra of the rare gas films were taken with the white light continuum of a Xe arc lamp, focused onto the ClF/Ar sample and afterwards collimated on the fiber optic spectrometer. The broad absorption of ClF was too weak to distinguish it from the scattered light that increases towards the UV. As the UV light dissociates ClF, a change in optical density of the sample is observed, which is probably due to absorption at 320 nm from the ClF_2 species generated [173], or due to bleaching of the Cl_2 absorption at 330 nm (Fig. 2.12). Since the absorption of ClF in rare gas matrix could not be determined experimentally, the gas phase absorption is compared to calculations in chapter 5.1.2.

4.1.2 Emission from valence states

Excitation of ClF in Ar with a concentration of 1:1000 at 290 nm into the repulsive $^1\Pi_1$ state ($h\nu_1$ in Fig. 4.1) leads to a fluorescence spectrum shown in Fig. 4.2a. The vibrational progression with 9 peaks ranging from 600 to 950 nm indicates recombination within the cage and emission from the bound $^3\Pi$ states. The corresponding spin-flip occurs within less than 500 fs (cf. chapter 7.6). Only one progression is observed in the spectrum, suggesting that vibrational relaxation is completed within the radiative lifetime. Indeed, the assignment in the discussion (Sect. 5.1) shows that the spectrum corresponds to transitions from $v' = 0$ in the A' state to a series of v'' levels in the electronic ground state ($h\nu_2$ in Fig. 4.1). Increasing the ClF concentration from dilutions of 1:20000 up to 1:1000 results in an approximately linear increase of the fluorescence intensity and leaves the spectrum unchanged. It is therefore attributed to ClF monomers. A significant contribution from a broad background, probably originating from dimers and higher clusters, is observed only at concentrations as high as 1:500.

Changing the excitation wavelength to 308 nm yields spectrum b) in Fig. 4.2 which contains the same progression as for 290 nm but with a superimposed sequence of sharper lines. The additional lines were previously identified as the $A'\,(v' = 0) \rightarrow X\,(v'')$ vibrational progression of Cl_2 [191]. In the gas phase, the absorption cross section of Cl_2 exceeds that of ClF by a factor of 60 at 308 nm (Fig. 2.12). The rather similar intensities of the Cl_2 and ClF emissions in Fig. 4.2b are consistent with the specified 1% Cl_2 impurity content in the sample gas. At 290 nm the absorption cross sections become equal and so the Cl_2 lines are not visible in Fig. 4.2a. The Cl_2 emission lines are sharper than the ClF lines and the triplet structure due to the isotope splitting of Cl_2 [191] is well resolved. Thus the width of the ClF lines is not limited by the experimental resolution. There is no systematic trend of the bandwidths with v''; the line shape is predominantly Gaussian and the width (fwhm) obtained from the Gaussian fit is included in Tab. 4.1.

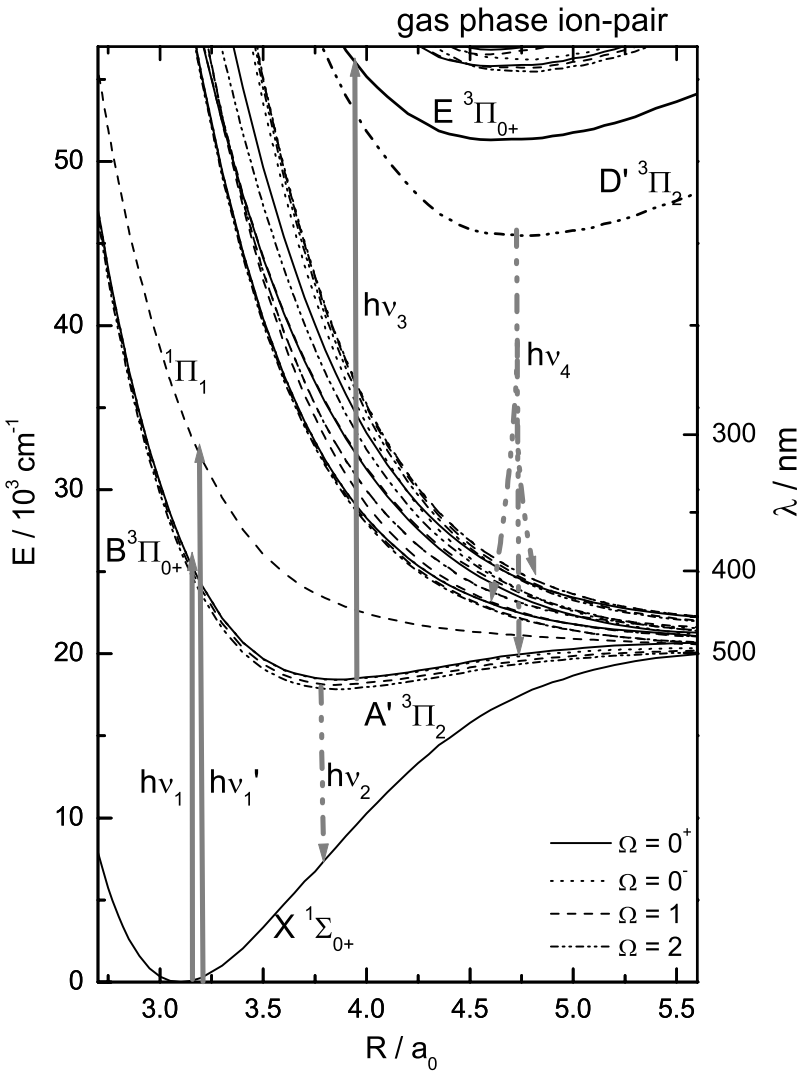

Figure 4.1: Potential diagram of ClF from ref. [121]. The line style indicates the Ω quantum number. All valence states are unshifted and the gas phase ion-pair energies are indicated on the top border of the plot. The E state is indicated with the shift in absorption (4500 cm^{-1}) and the emitting D' state with the shift in emission (10000 cm^{-1}). $h\nu_1$ and $h\nu_1'$ indicate the absorption to the B and $^1\Pi$ state that result in the emission band $A' \rightarrow X$ ($h\nu_2$). The excited state absorption $h\nu_3$ to the E state induces the emission band from D' with three contributions.

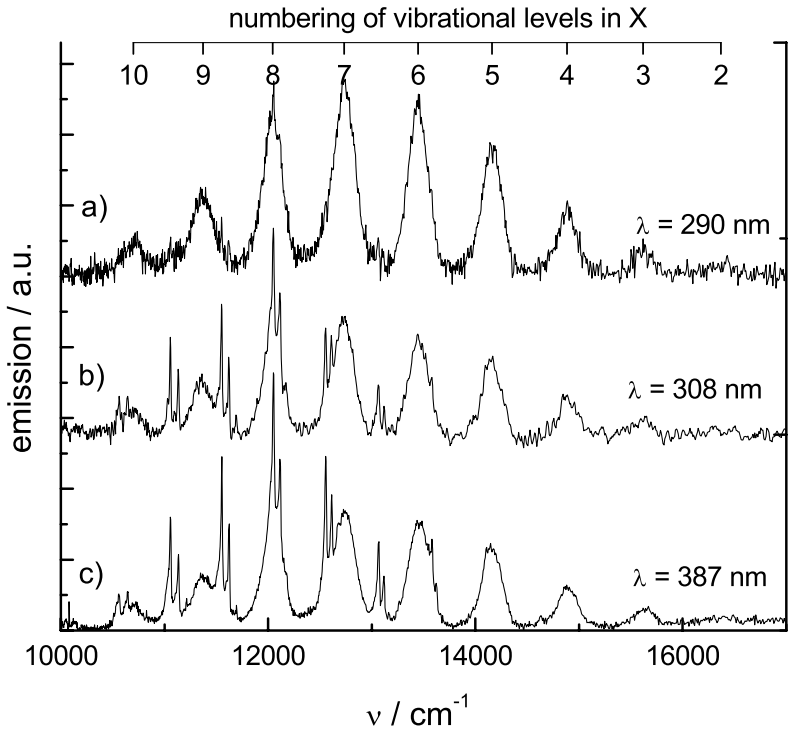

Figure 4.2: Vibrational progression of the $A' \rightarrow X$ fluorescence of ClF in Ar for different excitation wavelengths: $\lambda_{ex} = 290$ nm (a), 308 nm (b) and 387 nm (c). The numbers indicate the vibrational quantum number v'' in the X state (see chapter 5.1.1). The sharp peaks in the spectra for $\lambda_{ex} = 308$ nm and 387 nm are zero-phonon lines for the three isotopomers of Cl_2.

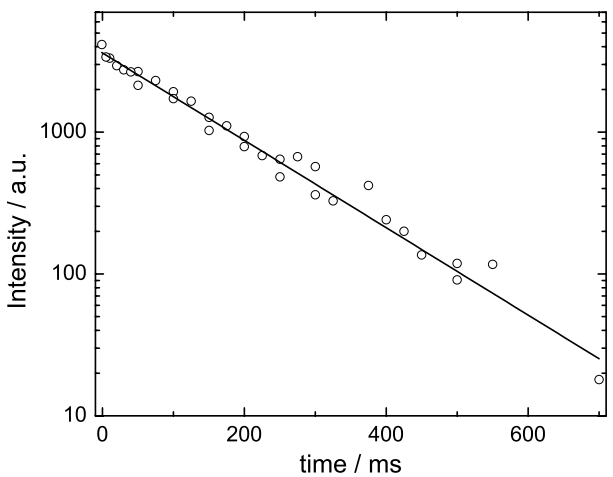

Figure 4.3: Intensity of the ClF fluorescence between 14,000 cm^{-1} and 15,100cm^{-1} as a function of time (see Fig. 4.2) after excitation at 308 nm. The solid line is an exponential fit to the data which yields the lifetime $\tau = 141 \pm 6$ ms.

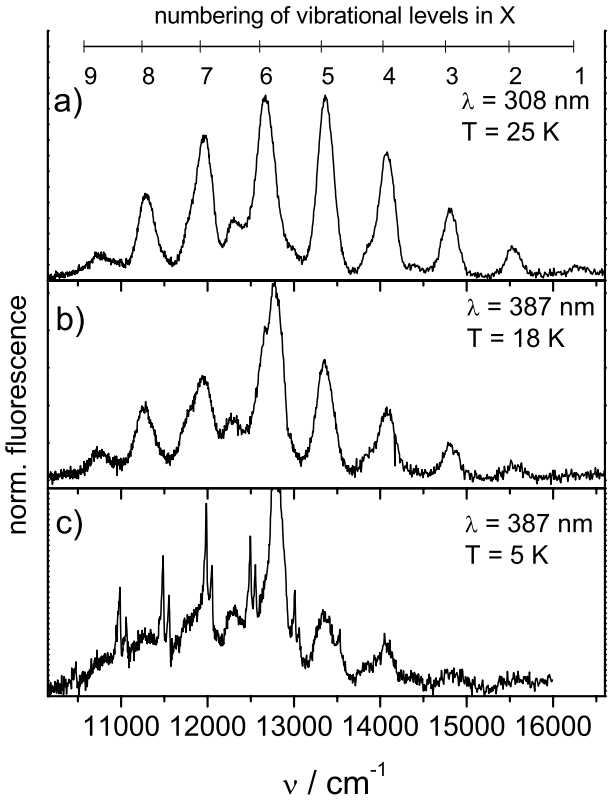

Figure 4.4: Vibrational progression of the $A' \rightarrow X$ fluorescence of ClF in Kr for different excitation wavelength. The sharp peaks in the spectrum for $\lambda_{ex} = 387$ nm at 5 K are zero-phonon lines for the three isotopomeres of Cl_2. a) $\lambda_{ex} = 387$ nm, $T = 5$ K, b) $\lambda_{ex} = 387$ nm, $T = 18$ K and c) $\lambda_{ex} = 308$ nm, $T = 25$ K.

With 387 nm radiation from the frequency doubled Ti:Sa laser the $B(^3\Pi_0)$ state of ClF ($h\nu_1'$ in Fig. 4.1) is excited. The same ClF fluorescence band is observed as with 308 nm excitation (cf. Fig. 4.2c), but the relative intensities compared to the Cl_2 lines are changed. Nonradiative relaxation populates the same excited state in ClF in the end, independent of the electronic valence state that is excited (cf. chapter 7.6).

The fluorescence lifetime has been measured by delaying the 50 ms integration window of the fiber spectrometer with respect to the excimer laser pulse. Fig. 4.3 shows a semi-logarithmic plot of the intensity of the two ClF bands between 14000 and 15100 cm^{-1}. In this range no contributions from Cl_2 spoil the spectra. The exponential fit yields a lifetime of 141 ± 6 ms. No significant contributions on shorter time scales could be found with the CCD camera, which has 1 μs time resolution. An additional quickly decaying component is observed for high concentrations only and attributed to Cl_2 containing dimers, since the fluorescence spectrum has the vibrational pattern of Cl_2 without isotopic splitting.

A similar but slightly red-shifted progression is observed in Kr matrix (Fig. 4.4) and the maxima of the transition energies in both matrices are listed in Tab. 4.1.

4.2 Ionic states of ClF, Cl_2 and excimers

To access the ionic states or the excimers, two photon excitation is needed. This is accomplished by tight focusing of the excimer laser or by a double-pulse sequence of femtosecond pulses with appropriate time delay.

4.2.1 Emission from Cl^+F^-

The tightly focused excimer laser excitation at 308 nm results in an additional fluorescence band around 420 nm (Fig. 4.5). Its structure and short wavelength are incompatible with emission from

	Ar		Kr	
v''	$\nu\,(v'')$	$\Delta\nu$	$\nu\,(v'')$	$\Delta\nu$
0				
1			16298	351
2	16368	250	15543	358
3	15619	240	14808	282
4	14883	257	14081	271
5	14159	225	13367	256
6	13446	233	12666	298
7	12735	250	11975	290
8	12044	232	11304	266
9	11371	282	10696	380
10	10701	274		

Table 4.1: Observed positions ν and widths (fwhm) $\Delta\nu$ in the emission from valence states to the ground state. All values are in cm^{-1}.

valence states since the only bound valence state would emit in the red range. The band can be decomposed into four contributions with Gaussian shapes and equal widths as shown in Fig. 4.5 and discussed in Sect. 5.2. The emission from valence states shown in Fig. 4.2 slowly bleaches with irradiation due to permanent ClF dissociation (see chapter 5.4). The three bands around 420 nm, except the fourth peak at 20,000 cm^{-1}, show exactly the same bleaching behavior as the red fluorescence band. Since the red bands unambiguously belong to ClF, the same holds true for the three blue emission bands, which must result from excitation of higher-lying ionic states. The ionic manifold can only be excited by a two-photon absorption of ClF ($h\nu_1$ and $h\nu_3$ in Fig. 4.1) and it is the only one in reach for two photons at 308 nm. This assignment is confirmed by the quadratic dependence of the emission intensity on the incident laser pulse energy. The fluorescence lifetime is measured with a combination of filters and a photomultiplier to be 50 ns. A lower bound for the gas-phase lifetime of $\tau = 15$ ns attributed to the D' state is given by the laser emission [165] with 3.3 bar buffer-gas pressure and a similar lifetime has been estimated from OODR experiments [147]. However a longer lifetime may be observed, when the D'-state is populated via the longer-lived $^3\Sigma^-$-state, which is excited in the present experiment. This has been detailed for the case of Cl_2 [166, 192]. In the condensed phase nonradiative electronic and vibrational relaxation within the ionic manifold is generally fast compared to the radiative decay. Therefore, the emission is attributed to dipole-allowed transitions from the lowest ionic state, $D'(^3\Pi_2)$ to the lower lying valence states ($h\nu_4$ in Fig. 4.1).

4.2.2 Emission from $Kr_2^+F^-$ exciplex and Cl^+Cl^-/Ar

The emissions reported in this chapter have already been observed and published. The aim of this spectroscopic study is to show how they can be excited with two femtosecond pulses, that will be used in pump-probe spectra.

$Kr_2^+F^-$ emission

The only excimer emission that could be exploited for pump-probe spectroscopy in this thesis originates from $Kr_2^+F^-$ and is displayed in Fig. 4.6a as the noisy line. This emission, centered around 460 nm, was previously assigned in ref. [54] and reproduced in Prof. Schwentner's group [82, 193]. Fig. 5.3 confirms that the $Kr_2^+F^-$ emission is observed in the present experiments. It is produced by two pulse excitation with $\lambda_{diss} = 387$ nm and $\lambda_{probe} = 270$ nm. The noisy line is the signal of a sample irradiated with λ_{diss} and λ_{probe} for 3 minutes to generate F by ClF dissociation and excite the KrF excimer. The spectrum of a virgin sample without F radicals is subtracted (not shown). The emission grows and saturates with irradiation time (cf. chapter 4.3.3). The shape of the emission is independent of the degree of ClF decomposition and only $\lambda_{probe} = 270$ nm is needed to excite the

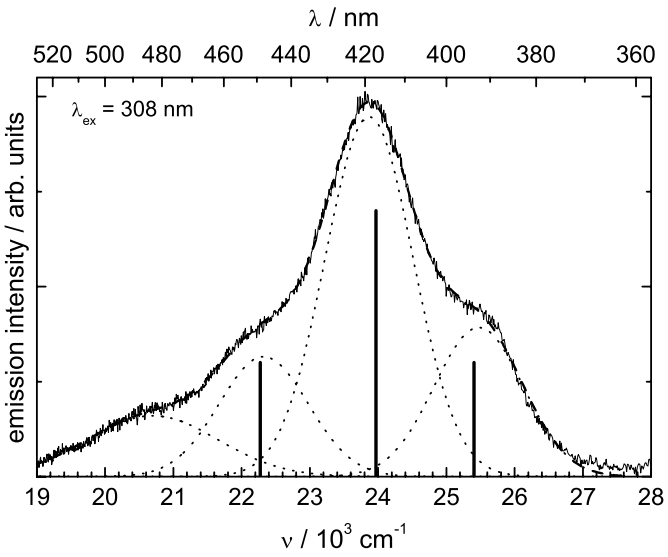

Figure 4.5: Fluorescence spectrum of the D' emission in Ar after two-photon excitation at $\lambda_{ex} = 308$ nm. The experimental spectrum (solid line) is fitted by four Gaussian functions whose superposition (dashed line) give excellent agreement with the measurement. The individual peaks are plotted as dotted lines. The vertical bars indicate the line positions calculated from the calculated gas-phase potentials [121] assuming a shifted D' state but unchanged valence states.

fluorescence after the sample was irradiated. This substantiates the assignment to a product of the dissociation. Since Cl containing products can be ruled out (see chapter 5.2.2), it must be assigned to a KrF species. The spectra can be fitted with two Gaussians centered around $\lambda_1 = 441$ nm and $\lambda_2 = 481.5$ nm. Fig. 4.6a displays the fit to the noisy line as thick dashed lines.

Fig. 4.6b collects spectra which represent the emissions that contribute to pump-probe signals that monitor the cage exit dynamics (chapter 7.7). They are the difference of the spectra taken for time delays between pump and probe of $\Delta t = 0$ ps (dashed), $\Delta t = 1.5$ ps (dotted) and $\Delta t = 100$ ps (solid), respectively, minus the spectrum recorded for $\Delta t = -1.5$ ps (not shown). These spectra correspond to three measured intensities in the pump-probe spectra in Fig. 6.13a. The differences are only 10% of the entire recorded signal (noisy line), and the spectra in Fig. 4.6b have been smoothed. The noisy line in panel a) thus represents the spectrum of all the KrF species that accumulated during the experiment and do not undergo recombination to ClF (see below). The 10% variation measures how this population of F atoms changes with the time delay of the pump-probe sequence on a timescale of ps. In the first 1.5 ps, the spectra differ mainly in the intensity of the Gaussian at 441 nm. After that, both bands are reduced by the same amount.

Fig. 4.7 shows a comparison of the $Kr_2^+F^-$ emissions for the accumulated populations created with $\lambda_{pump} = 387$ nm and $\lambda_{probe} = 270$ nm (thick lines) versus $\lambda_{probe} = 278$ nm (thin lines) in a temperature cycle. In both cases the sample is irradiated until the saturation of the emission growth is reached. While the signal intensity of the emission excited with $\lambda_{probe} = 270$ nm is halved upon raising the temperature from 4.5 K to 11 K and again from 11 K to 27 K. The intensity with $\lambda_{probe} = 278$ nm is reduced by a factor 5 from 4.5 K to 11 K and then halved for a further increase to 27 K. When the temperature is reduced to the initial 4.5 K, the intensity for $\lambda_{probe} = 278$ nm excitation recovers entirely. It does not recover instantaneously, but on the order of 20 seconds which is much faster than the initial growth saturating after ∼200 seconds. For $\lambda_{probe} = 270$ nm the emission only grows back to 75% of the initial value.

This behavior indicates that $\lambda_{probe} = 278$ nm probes F atoms in such sites in the Kr lattice which do not recombine to ClF by annealing. Warming up the sample leaves the F atoms very near the site, where they have been trapped after dissociation. On the other hand, $\lambda_{probe} = 270$ nm probes F atoms that can disappear from their site by thermal migration.

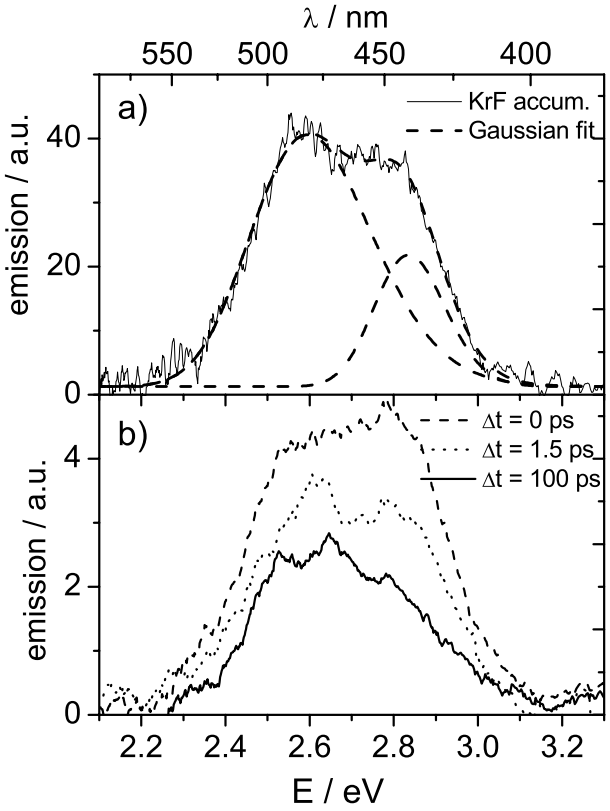

Figure 4.6: a) $Kr_2^+F^-$ emission from the accumulated population, excited with a double pulse sequence of 387 + 270 nm, is shown as a noisy line and fitted with the sum of two Gaussians centered at 441 and 481.5 nm. b) The spectra show the change of the fluorescence band for excitation with time delay $\Delta t = 0$ (dash) 1.5 (dotted) and 100 ps (solid) with respect to excitation with $\Delta t = -1.5$ ps.

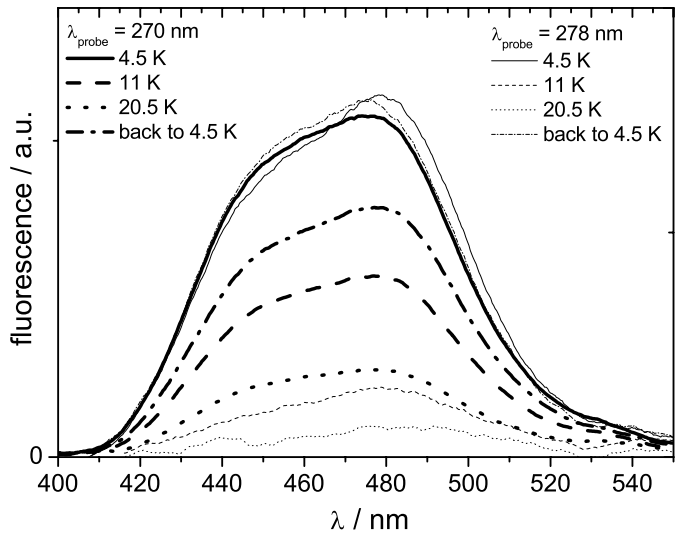

Figure 4.7: $Kr_2^+F^-$ emission from the accumulated population excited with a double pulse sequence of $\lambda_{pump} = 387$ nm and $\lambda_{probe} = 270$ nm (thick lines) vs. $\lambda_{probe} = 278$ nm (thin lines). Starting from 4.5 K (solid) the temperature is decreased to 11 K (dashed) and 20.5 K (dotted). Subsequently, the temperature is lowered again to 4.5 K. While the spectrum for $\lambda_{probe} = 278$ nm gains back the full intensity, 25% are lost for $\lambda_{probe} = 270$ nm. Note that the temperature dependence for $\lambda_{probe} = 278$ nm is much stronger.

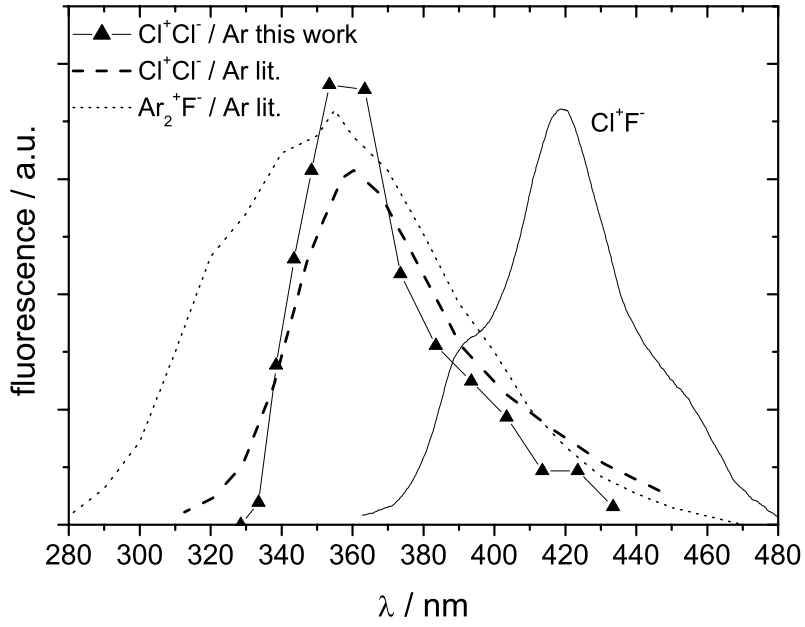

Figure 4.8: The solid triangles show the fluorescence spectrum measured after two pulse excitation with $\lambda_{pump} = 290$ nm and $\lambda_{probe} = 280$ nm. It is attributed to the D' emission of Cl^+Cl^-/Ar (thick dashed [134, 194]). It is observed in pure Cl_2/Ar matrices as well as in ClF/Ar samples due to the 1% Cl_2 content. For comparison the dotted line shows the $Ar_2^+F^-$ emission [81, 83]. The solid line reproduces the Cl^+F^- emission from Fig. 4.5.

$Ar_2^+F^-$ vs. Cl^+Cl^-/Ar emission

The analog emission in Ar matrices, i.e. fluorescence from $Ar_2^+F^-$, is reproduced in Fig. 4.8 from ref. [81] as the dotted line. It is centered around 355 nm and was excited by 193 nm pulses after dissociation of F_2 in Ar. An excitation spectrum of the $Ar_2^+F^-$ emission in ref. [83] shows a threshold of the absorption at 6 eV, corresponding to 208 nm.

In this thesis, a very similar emission is produced by excitation with a 290 nm + 280 nm pulse sequence and is plotted in Fig. 4.8 as solid triangles. The same emission can be produced by 387 nm + 280 nm excitation, but then the stray light from the 387 nm pulses spoils the spectra. In ref. [195] it was attributed to the $Ar_2^+F^-$ emission, and the surprisingly low excitation threshold of 286 nm was argued to be conceivable for hot F atoms. A large energy of 1.3 eV would be gained in the ionic state of Ar^+F^- upon compression of the $Ar - F$ bond from 0.35 to 0.24 nm [51] (cf. the corresponding KrF potential in Fig. 5.5). However, this argument neglects that even in the largest interstitial site the ArF bond is already compressed to 0.29 nm and the energy gain can only be half as high.

An intriguingly similar emission at 360 nm was reported for Cl^+Cl^-/Ar and it is reproduced in Fig. 4.8 as a dashed line [134, 194]. The agreement with the curve measured in this thesis (triangles) is good but not perfect. Therefore this new assignment was confirmed by preparing pure Cl_2/Ar samples. The same emission is observed, corroborating the assignment to Cl^+Cl^-/Ar. In the ClF doped samples this emission originates from the 1% content of Cl_2 in the ClF gas. It is observed with similar intensity as the Cl^+F^- emission, since the first step in the pump-probe sequence is the much stronger Cl_2 absorption shown in 2.12. Fig. 5.7 demonstrates that the absorption threshold of

286 nm observed in this thesis is consistent with the calculated potential surface of Cl_2, when the ionic state is red shifted as for ClF/Ar.

4.2.3 Excited state absorption of ClF and Cl_2

To locate the energy of the ionic states Cl^+F^- in absorption, two-photon excitation was performed with tunable radiation from the frequency doubled NOPAs (chapter 3.5.2). Since the minima of the ionic states are significantly displaced with respect to the bound valence states A', A and B, as shown in Fig. 2.11, vertical excitation of a vibrationally relaxed population in the bound valence states with 308 nm would not reach the minimum of any ionic state. However, frequency-doubled pulses from the Ti:Sa laser at $\lambda_{pump} = 387$ nm and 110 fs duration excite ClF into the B state somewhat above the dissociation limit ($h\nu_1'$ in Fig. 4.1). A time-correlated second UV pulse (probe) from a frequency-doubled NOPA excites the population from the triplet valence states into the ionic triplet states, provided as the probe-photon energy is larger than the minimum of the difference potential ΔV between the triplet valence and ionic states. The resonance condition [23, 45] for the probe photon is determined by the difference potential ΔV only and not by adding the energies of the pump and the probe photons (cf. chapter 2.3.2). The NOPA probe wavelength is tuned while recording the blue emission intensity at 420 nm. The onset of the blue emission is found at a probe wavelength of 322 nm, or $\Delta V = 31055$ cm^{-1}. The lowest transition allowed by the selection rules connects the $B(^3\Pi_0)$ state to the $E(^3\Pi_0)$ state. Comparing the measured ΔV with the gas phase value, and allowing for a vertical shift of the calculated potentials [121] in the matrix due to polarization, a red-shift of 4500 cm^{-1} is derived, i.e. $T_e\,(E)_{abs} = 51321$ cm^{-1}. Assuming an equal vertical shift also for the lowest ionic state, i.e. the D' state (Fig. 4.1), the energy minimum for the ionic manifold is 50750 cm^{-1} or 6.29 eV which is included in Tab. 5.1 as $T_e\,(D')_{abs}$.

The same strategy is pursued for Cl_2/Ar. The sample is pumped with the 387 nm pulse. The emission from Cl^+Cl^-/Ar at 360 nm is monitored while tuning the time-delayed UV pulse. The onset of the excitation spectrum is found at 286 nm. With the same arguments as above, the minimum of the E state of Cl_2 in Ar is red shifted by 3758 cm^{-1} to $T_e(E) = 38723$ cm^{-1}.

4.2.4 Absorption of KrF

The excimer absorption that leads to the above mentioned $Kr_2^+F^-$ emission is presented in Fig. 4.9b. It is recorded by measuring the transmission of a ClF/Kr sample at various temperatures with the white light spectrum of a focused Xe arc lamp. The white light dissociates ClF and detects the absorption of KrF simultaneously. The ratio of the transmission before and after bleaching the sample with the white light yields the plotted spectra. For each temperature a fresh spot on the sample was selected and irradiated for 5 min. The thick solid line shows another spectrum at 4 K, which was taken after 30 min irradiation.. The comparison in 4.9a to the excitation spectra of the $Kr_2^+F^-$ emission reported in refs. [82, 193] and [88] demonstrates the assignment to the KrF absorption, which yields the emission at 460 nm (Fig. 4.6).

While the excitation spectrum reported by Apkarian for $T = 12$ K (thick line in panel a), excited with frequency-doubled dye laser, resembles the cold spectrum which was irradiated for 25 min (thick line in panel b), the spectrum due to Bressler (thick dashed line panel a), excited with synchrotron radiation, resembles the one taken at 27 K with only 5 min irradiation. Another absorption spectrum of KrF/Kr at 22 K is available in the literature [132], and it shows a similarly broad absorption peaking at 265 nm.

In summary, the KrF absorption, that generates the $Kr_2^+F^-$ emission, depends on temperature and on irradiation time (photon flux). High temperatures and low photon flux preferentially produce a broad absorption in the range 250 - 270 nm. Cold temperatures together with long irradiation time or high photon flux create a narrow absorption centered at 275 nm.

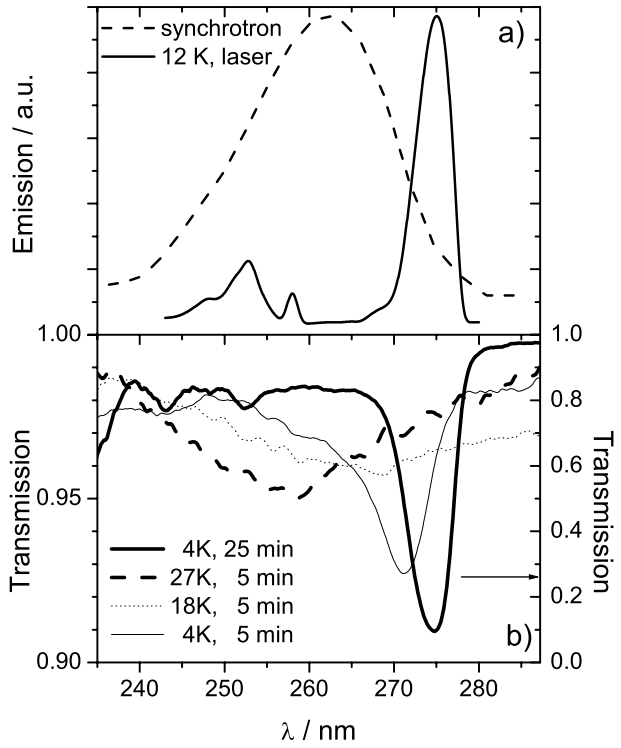

Figure 4.9: a) Excitation spectra of KrF measured by detection of the $Kr_2^+F^-$ emission. The solid line is reproduced from ref. [54] (laser excitation at 12 K) and the dashed line from ref. [82, 193] (synchrotron excitation, no temperature given). b) The transmission of ClF doped Kr samples measured in this thesis shows the absorption at 275 nm after 30 min irradiation at 4 K (thick solid line, right hand scale). The left hand scale is for 5 min irradiation. 27 K (thick dashed) yields an absorption similar to the dashed excitation in panel a). 18 K (thin dotted) and 4 K (thin solid) result in intermediate absorption bands.

4.3 Photobleaching of ClF in Ar and Kr

To prepare for pump-probe investigations on the cage exit dynamics of the F atom, experiments concerning the dissociation quantum efficiencies ϕ and their dependence on the kinetic energy of the F atom and the sample temperature are also carried out. These static measurements are partly performed with a $XeCl$ excimer laser and yield permanent dissociation efficiencies, i.e. the probability that an initially excited molecule will permanently dissociate and not recombine. The fluorescence signal, which is indicative of the remaining ClF concentration, changes on a timescale of seconds to minutes, depending on the photon flux. In contrast, fs-pump-probe experiments and molecular dynamics simulation only follow the processes over several ps. Thus processes like diffusion, occurring on longer timescales, are not included in fs experiments and simulations. In this chapter the permanent dissociation efficiency is measured, which is naturally smaller than dissociation efficiencies determined on the ps-timescale.

4.3.1 Bleaching of ClF/Ar

Excitation at 308 nm into the repulsive $^1\Pi_1$ state leads to permanent dissociation of ClF. This is monitored by the red fluorescence bands attributed to $A' \rightarrow X$ emission of ClF (see Sect. 5.1), which is proportional to the remaining ClF concentration. The decay of this red emission versus irradiation at 308 nm is shown in Fig. 4.10 for ClF in Ar (1:50,000) at a matrix temperature of 5 K. An exponential decay with 15% offset perfectly fits the measured trace. The reason for the offset cannot be unambiguously assigned. While there may be a weak background fluorescence from impurities like Cl_2, it is most likely due to reformation of ClF induced by secondary photodissociation of species that are formed by the migrating F atoms, such as F_2, ClF_2, ClF_3 etc.

A concentration study was performed to clarify the influence of secondary reactions. For the range of concentrations from 1:1,500 to 1:100,000, plotted in Fig. 4.11, the decay is only slightly slower for lower concentrations. For the discussion of the photodissociation quantum yield (chapter 5.4.1)

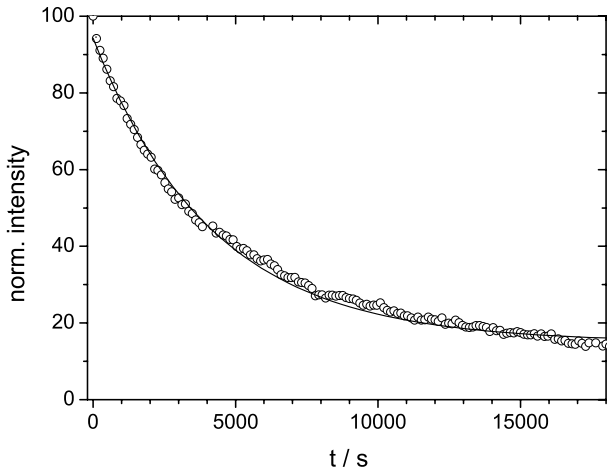

Figure 4.10: Intensity of the $A' \rightarrow X$ emission versus irradiation time at constant intensity for excitation of ClF in Ar (1:50,000) at 308 nm and 5 K. This intensity is a measure of the ClF concentration remaining in the sample. The solid line is an exponential fit to the experimental points with a background of 15%.

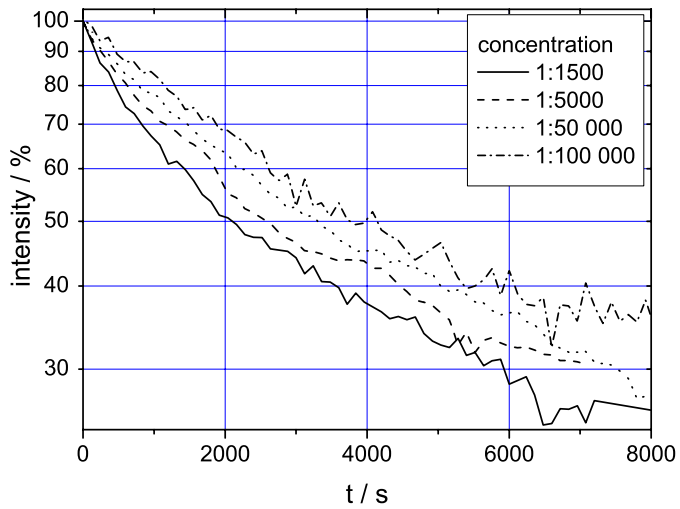

Figure 4.11: Intensity of the $A' \rightarrow X$ emission on a logarithmic scale versus irradiation time at constant intensity for excitation of ClF in Ar at 308 nm and 5 K. The concentration is varied from 1:1500 to 1:100000. Higher concentrations yield a faster initial decay and a stronger deviation from exponential decay.

the main (i.e. early) part of the decay curves is fitted with single exponentials. The resulting decay constants k allow the calculation of the dissociation cross section $\sigma\phi_d = k/I$, where I is the photon flux and $\sigma\phi_d$ is the product of the absorption cross section σ and the permanent dissociation efficiency ϕ_d. The lowest concentration (1:100,000) at 5 K yields the dissociation cross section $(\sigma\phi_d)_{308} = 1.5 \times 10^{-22}$ cm^2, which increases by a factor of 1.7 in going to a concentration of 1:1,500. Increasing the temperature of the matrix to 19 K (still below the thermal mobility of F in argon) enlarges the dissociation efficiency at 308 nm by 14%.

Excitation of ClF at 308 nm prepares the F atom with a substantial kinetic energy of $E_{kin} = 0.9$ eV. The gas phase dissociation energy of 20930 cm^{-1} corresponds to 478 nm. A wavelength of 387 nm from the frequency-doubled Ti:Sa laser yields $E_{kin} = 0.4$ eV. Once more a significant bleaching is observed. From a single-exponential fit the dissociation cross section $(\sigma\phi_d)_{387} = 2.1 \times 10^{-23}$ cm^2 is obtained at a concentration of 1:20,000.

The bleaching of ClF (Fig. 4.10) clearly demonstrates permanent dissociation of ClF and therefore also the mobility of the F fragment in Ar matrices. As mentioned above, the offset and the deviation of the decay curves in Fig. 4.11 from a single-exponential, indicate back reaction or other secondary reactions (see chapter 5.4). Such reactions will in general lead to a faster decrease for

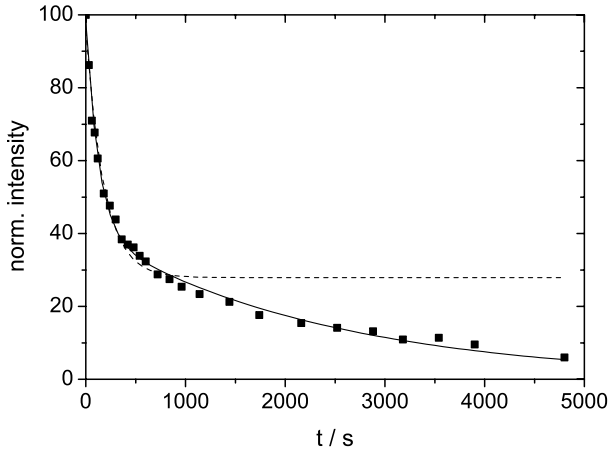

Figure 4.12: Intensity of the $A' \rightarrow X$ emission versus irradiation time at constant intensity for excitation of ClF in Kr at 308 nm and 28 K at a concentration of 1:5000. The dashed line is a single exponential fit with 28 % background. The solid line is a double exponential fit without background.

early times since rate constants add up, whereas at later times the slope might be smaller due to back reactions of newly formed species. This behavior is observed in the concentration study in Fig. 4.11, which shows a faster decay in the beginning for higher concentrations. Also optically thick samples will result in non-exponential decay and a constant offset for long times.

The concentration and the thickness d of the samples were lowered as much as possible to ensure optically thin and clear samples and to reduce secondary reactions while maintaining a reasonable signal-to-noise ratio. However, even at the lowest concentrations of 1:100,000 ($d = 50$ μm) used here, the decay deviates from a single exponential or shows an offset. The slopes at early and late times (or low and high doses) give limits to the true dissociation rate. At a concentration of 1:50,000 the early slope is 2.5×10^{-4} s^{-1} and the slope for long bleaching times is 0.75×10^{-4} s^{-1}. At an intensity $I = 1.4 \times 10^{18}$ photons·s^{-1}·cm^{-2} these slopes result in values of $(\sigma\phi_d)_{308} = 1.8 \times 10^{-22}$ cm^2 and 6.3×10^{-23} cm^2 for short and long bleaching times, respectively. The value from a single-exponential fit lies in between at 1.6×10^{-22} cm^2.

4.3.2 Bleaching of ClF in Kr

A similar bleaching study for ClF/Kr at 28 K and 308 nm for a concentration of 1 : 5000 is shown in Fig. 4.12. The deviation from exponential decay is even stronger. A single exponential fit to the early decay with 28 % background (dashed line) yields a close approximation. The resulting dissociation cross section is $(\sigma\phi_d)_{308} = 1.3 \times 10^{-21}$ cm^2. However, only a double exponential fit without offset (solid line) reproduces the entire curve. From the faster initial decay the cross section $(\sigma\phi_d)_{308} = 1.8 \times 10^{-21}$ cm^2 is obtained. This dissociation cross section is an order of magnitude larger than the one observed in Ar. Also, the dissociation cross sections for 387 nm excitation, $(\sigma\phi_d)_{387}$, are a factor 10 larger in Kr than in Ar (see Tab. 5.4). The next chapter will show that in Kr not only photoexcitation of the molecules formed after dissociation such as F_2, ClF_2 and ClF_3 leads to mobilization of F fragments, but also the excitation of the KrF exciplex.

In Kr the F atoms become thermally mobile at 15 K [81]. A large mobility is also seen in experiments with tightly focused lasers as they are used for the fs-pump-probe experiments. A pulse at 387 nm dissociates ClF in Kr in a spot of 100 μm diameter and a probe pulse at 270 nm is spatially overlapped to produce the $Kr_2^+F^-$ emission (Fig. 4.6) by exciting the F fragments in Kr. The emission rapidly grows as ClF is dissociated. After some time, however, it saturates and slowly decays. This already indicates, that F atoms are either trapped by impurities to form a molecule, which are not re-exited, or the F atoms leave the irradiated volume. In a warm sample (~ 25 K) the latter process is clearly proved to give a large contribution to the signal decay. When the sample is

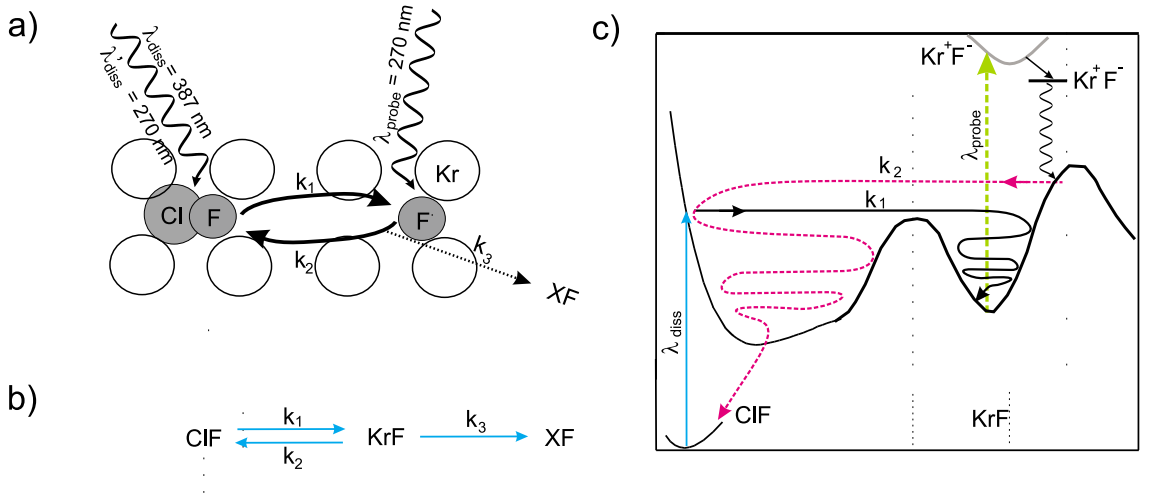

Figure 4.13: a) Scheme depicting the reversible shutteling of F atoms from Cl to Kr. $\lambda_{diss} = 387$ nm and $\lambda'_{diss} = 270$ nm dissociate ClF, leading to KrF species with a rate constant k_1. $\lambda_{probe} = 270$ nm drives the recombination to ClF with the rate constant k_2 by inducing the radiative dissociation of $Kr_2^+F^-$ (see text). The rate k_3 collects all processes that remove F from this reversible process. b) Rate model. c) Reversible photo process from ClF to KrF in a potential diagram (see text).

moved after long irradiation of a 100 μm large spot, the $Kr_2^+F^-$ fluorescence rises considerably just next to the focus, while it decreases to zero on a fresh spot. This clearly indicates that the F atoms are transported in the solid over macroscopic distances on the order of tens of micrometers by repeated re-excitation.

4.3.3 Control of dissociation vs. recombination of ClF in Kr

The configuration with two pulses, a dissociation pulse at $\lambda_{diss} = 387$ nm and a probe pulse at $\lambda_{probe} = 270$ nm is used for further investigations. The latter pulse contributes to the dissociation of ClF via the $^1\Pi_1$ state and is referred to as $\lambda'_{diss} = 270$ nm. More importantly, the probe pulse at $\lambda_{probe} = 270$ nm produces the emission from the $Kr_2^+F^-$ exciplex, which terminates on a repulsive KrF potential and provides the F fragments with substantial kinetic energy (radiative dissociation of $Kr_2^+F^-$), driving the recombination of F fragments with the immobile Cl radicals. Fig. 4.13a summarizes these processes schematically. Both $\lambda_{diss} = 387$ nm and $\lambda'_{diss} = 270$ nm dissociate ClF and lead to a KrF configuration with a rate constant k_1. $\lambda_{probe} = 270$ nm produces the $Kr_2^+F^-$ emission, which is observed in the experiments and leads to reformation of ClF with the rate constant k_2. A constant k_3 collects all processes that remove F atoms from this reversible process, e.g. by promoting F out of the laser focus. Fig. 4.13b restates this rate model. A schematic representation of the reversible process is shown in the potential diagram in Fig. 4.13c. Starting from the ground state of ClF, λ_{diss} dissociates the molecule and the F fragment must overcome the cage barrier. When it is cooled down in the Kr cage, λ_{probe} excites the ion-pair state Kr^+F^-. After rearrangement in the ionic manifold the $Kr_2^+F^-$ exciplex fluoresces (wavy arrow). The emission terminates on a repulsive KrF surface and the F fragments can overcome the barrier in the other direction to finally recombine to ClF.

Fig. 4.14a shows the $Kr_2^+F^-$ emission as a function of irradiation time in seconds for a Kr matrix doped with ClF at a concentration of 1:1000. In the first 400 s only the 270 nm laser is present, and thus responsible both for the dissociation λ'_{diss} and the probing λ_{probe}, which also drives recombination. The concentration of F fragments, i.e. KrF species, grows until it reaches a saturation value, which corresponds to an equilibrium of ClF dissociation versus recombination ($\lambda'_{diss} + \lambda_{probe}$). This

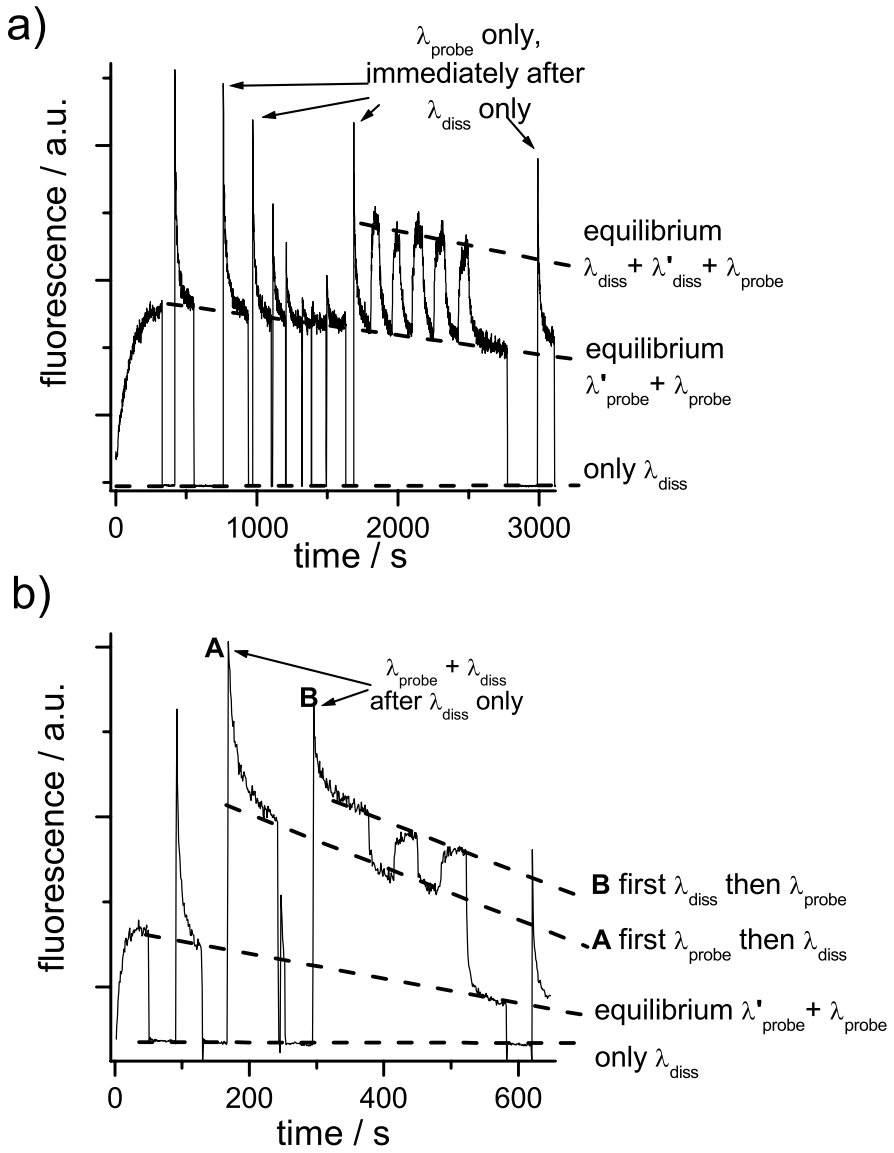

Figure 4.14: Concentration of F fragments measured via the $Kr_2^+F^-$ emission as a function of irradiation time with $\lambda_{diss} = 387$ nm and/or $\lambda_{probe} = 270$ nm (see text). The temperature is 4 K. Panel a) demonstrates how the photochemical equilibrium is shifted towards ClF by applying λ_{probe} and towards KrF with λ_{diss}. Panel b) demonstrates the effect of the time delay between λ_{diss} and λ_{probe} (see text).

equilibrium, indicated by the dashed line ($\lambda'_{diss} + \lambda_{probe}$), slowly decays in the course of the experiment according to the rate k_3. XF indicates the F fragments that leave the focus or that react to ClF_2 etc. The initial exponential growth curve can be fitted to determine the quantum efficiency (see chapter 5.4.1).

The dissociation laser $\lambda_{diss} = 387$ nm does not produce the excimer. When the signal in Fig. 4.14a drops to zero only the dissociation laser λ_{diss} is present and the second laser λ_{probe} is blocked. From 400 s to 1700 s, the sample is irradiated alternatingly with the dissociation laser only ($\lambda_{diss} \rightarrow$ no signal) and then with the probe laser only ($\lambda_{probe} \rightarrow$ spike). Obviously, after 400 s not all ClF molecules were dissociated in the equilibrium of $\lambda'_{diss} = \lambda_{probe} = 270$ nm, although the exponential growth converges. The dissociation pulse $\lambda_{diss} = 387$ nm can double the number of F fragments, depending on the time period used for dissociation.

From 1700 to 2500 s, λ_{probe} probes the sample continuously and λ_{diss} is switched on and of in addition. This switches the F fragment concentration from the equilibrium value for ($\lambda'_{diss} + \lambda_{probe}$) to a new equilibrium for both lasers ($\lambda_{diss} + \lambda'_{diss} + \lambda_{probe}$). The fluorescence is proportional to the number of F radicals. Approximately 30% of the F atoms are shuttled from Cl to Kr and back by switching λ_{diss} on and off, as can be estimated from the difference of the equilibria in Fig. 4.14a.

Fig. 4.14b shows a similar experiment, with higher laser intensity to demonstrate a more sophisticated effect. Again, in the first 50 s, the equilibrium concentration of F atoms for irradiation with $\lambda'_{diss} = \lambda_{probe} = 270$ nm is produced. The first spike at 90 s is generated in the same way as the first in peak in panel a) between 400 s and 1700 s. For the next two spikes at 170 s and 300 s, λ_{probe} is incident together with the dissociation laser λ_{diss} and the only difference is the time sequence between λ_{diss} and λ_{probe}. In sequence A λ_{probe} comes 1 ps before λ_{diss} and in sequence B λ_{probe} comes 100 fs after λ_{diss}[1]. From 400 s to 580 s, the time delay is switched four times and the fluorescence changes accordingly between the equilibria A and B, indicated on the right side of Fig. 4.14b. This peculiar behavior demonstrates a change of the equilibrium concentration of F radicals with time delay between λ_{diss} and λ_{probe}, which is discussed in chapter 5.4.2.

[1]Note that the repetition rate of both lasers is 1 kHz, i.e. the next sequence is 1 ms apart.